symmetry

MDPI

Article

Design of Broadband and Wide-Angle Hexagonal Metamaterial Absorber Based on Optimal Tiling of Rhombus Carbon Pixels and Implantation of Copper Cylinders

Yongjune Kim[1,*] and Jeong-Hae Lee [2,*]

[1] Metamaterial Electronic Device Research Center, Hongik University, Seoul 04066, Korea
[2] Department of Electronic and Electrical Engineering, Hongik University, Seoul 04066, Korea
* Correspondence: yjkim7826@hongik.ac.kr (Y.K.); jeonglee@hongik.ac.kr (J.-H.L.)

Abstract: A design method for a broadband and wide-angle metamaterial absorber is proposed based on optimal tiling of rhombus carbon pixels on and implantation of metal cylinders inside an acrylic substrate for which the backside is blocked by the perfect conductor. First, an intermediate carbon metapattern is achieved via optimal tiling of rhombus carbon pixels based on the genetic algorithm (GA), which can minimize the reflectances of both of the transverse electric (TE) and transverse magnetic (TM) polarized electromagnetic (EM) waves for the incident angles 0° and 60° simultaneously. Then, copper cylinders are implanted inside the substrate to boost the absorptions of both of the TE and TM polarizations for the 60° oblique incidences. To extend the absorption bandwidth, the design is finalized by evolving the intermediate metapattern using the GA. Based on the finalized carbon metapattern, the 90% absorption bandwidth is confirmed in the frequency range 8.8 to 11.6 GHz, for which the fractional bandwidth is 27.5% for both of the two polarizations with the incident angles from 0° to 60°. The proposed method could open a way to design a broadband and wide-angle EM metamaterial absorber that can be applied to the edges of three-dimensional structures such as a regular tetrahedron or square pyramid that have interior angles of 60° that cannot be covered by conventional square or rectangular metamaterial absorbers.

Keywords: hexagonal metamaterial absorber; broadband; wide angle; rhombus tiling; carbon; copper cylinders; genetic algorithm

Citation: Kim, Y.; Lee, J.-H. Design of Broadband and Wide-Angle Hexagonal Metamaterial Absorber Based on Optimal Tiling of Rhombus Carbon Pixels and Implantation of Copper Cylinders. *Symmetry* **2021**, *13*, 2045. https://doi.org/10.3390/sym13112045

Academic Editor: Kensuke Ogawa

Received: 4 October 2021
Accepted: 28 October 2021
Published: 30 October 2021

1. Introduction

Electromagnetic (EM) metamaterials are engineered artificial structures that can realize untapped ranges of constitutive parameters such as negative permittivity and/or permeability [1–3]. By utilizing the extreme properties of metamaterials, many intriguing applications have been reported such as miniaturized antennas [4–7], invisibility cloaks [8–12], and EM absorbers [13–31]. Among them, EM metamaterial absorbers are related with controlling the power of the incident EM wave, which can be connected to many potential applications such as sensing [14,17,25], imaging [18,22], stealth technologies [19,21], or energy harvesting [17,24]. In general, the EM metamaterial absorbers consist of a conductive pattern combined on a dielectric substrate blocked with a metallic sheet. The configuration enables resonances of EM fields inside the substrate, which can maximize the dielectric loss in it as well as the ohmic loss in the conductive pattern. By utilizing the loss mechanisms as well as matched impedance of the full structure to that of the free space via the conductive metapattern, perfect absorption can be achieved [13,14].

Even though the absorbing performances of the EM metamaterial absorbers have been verified successfully, they have long been captivated in the concept that the shapes of the side boundary of them are square or rectangular. The conventional shapes may limit their applications especially for three-dimensional (3D) structures such as the regular tetrahedron or the square pyramid that have interior angles of 60°. Because it is impossible

to tile the square or rectangular unit cells continuously near the edges of the structures, the periodic condition for the metamaterial absorber may not be satisfied, which is assumed in the design and necessary to realize the original performance of it. However, a unit cell with a regular hexagonal boundary can be applied at the edges maintaining the periodicity because the angle between two intersecting lines that connect the centers of the adjacent unit cells is 60° [30]. Even though hexagonal EM metamaterial [15,30] or frequency selective surface (FSS) [32] absorbers have been reported utilizing a dual-electric resonator [15], tiling of hexagonal carbon pixels [30], and resistively loaded quadruple hexagonal loops [32], there exist limitations that the absorption bandwidths of them are quite narrow especially for oblique incidences. For instance, an absorbing bandwidth of one of the referenced papers is abruptly deteriorated for the incident angle 45° [32].

In this study, a design method for a hexagonal metamaterial absorber is proposed that optimally tiles rhombus carbon pixels on an acrylic substrate of which the backside is blocked by the perfect conductor (PEC). To find the optimal metapattern, the genetic algorithm (GA) [33,34] is adopted for tiling the rhombus carbon pixels by linking it with the full-wave simulation. For the optimization at the X band, the figure of merit (FOM) of the GA is set to the average of the reflectances at 8, 10, and 12 GHz for the normal and 60° oblique incidences of the EM waves with two orthogonal transverse electric (TE) and transverse magnetic (TM) polarizations. By repeating GA operations until FOM is converged, an intermediate carbon metapattern is found. Then, copper cylinders are implanted inside the substrate to boost the absorptions for both of the TE and TM polarizations with 60° oblique incidences. Finally, an optimal metapattern is found by adaptively applying the GA on the intermediate carbon metapattern combined with implanted copper cylinders. Based on the full-wave simulation, the 90% absorption bandwidth is confirmed from 8.8 to 11.6 GHz, of which the fractional bandwidth is 27.5% for both of the TE and TM polarizations with the incident angles from 0° to 60°.

2. Design Method for Broadband Absorption

As an initial step, the unit cell of the hexagonal metamaterial absorber is discretized into small rhombus pixels as shown in Figure 1a. By tiling the rhombus pixels instead of hexagonal [30,35] or triangular pixels, it is possible to increase the diversity of the metapattern or to reduce the design complexity, respectively. Even though other polygons such as pentagons [36] can be utilized for the tiling accompanying an air-filled blank near the hexagonal boundary, they cannot guarantee the axial symmetry of the pattern inside the unit cell, which is necessary to reduce the design complexity as well as to maintain the polarization insensitivity for the normal incidence. Here, it is supposed that the metapattern composed of carbon rhombus pixels is attached on an acrylic substrate of which the height h_s is 4 mm and relative permittivity is about 2.6-i0.01 at 10 GHz [37]. The electrical thickness of the substrate is $0.22\lambda_g$ at 10 GHz, which is almost a quarter of the wavelength, where λ_g is the wavelength inside the acrylic substrate. The condition enables forming the quarter-wavelength standing wave inside the substrate of which the backside is blocked with PEC, which can induce resonant electric currents in the carbon metapattern and maximize the ohmic losses in it [38]. Here, the length of one side of the rhombus pixel l_p is set to 0.5 mm. The length of one side of and the distance between two parallel sides of the hexagonal unit cell are set to 7.5 and 12.99 mm, which are indicated by l_s and l_u, respectively. Because the distance between the center points of the adjacent hexagons is the same with l_u, the periodicity of the unit cell can be considered as 12.99 mm, which is about 0.52 λ_{min}, where λ_{min} is the wavelength in free space at the maximum frequency 12 GHz of the X band (8–12 GHz).

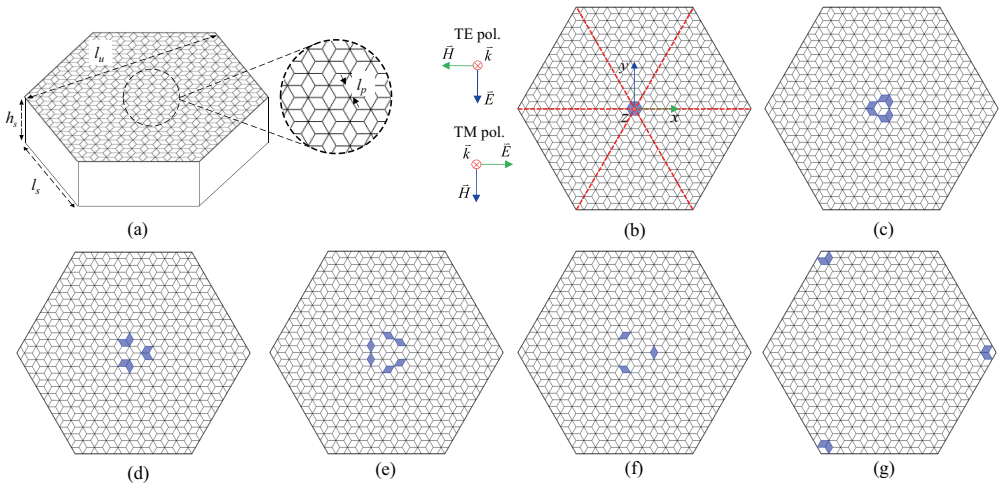

Figure 1. Schematic of a hexagonal metamaterial absorber unit cell discretized with rhombus pixels, for which h_s, l_s, and l_u are 4, 7.5, and 12.99 mm, respectively. Axially symmetric rhombus pixels are grouped as a pair and presented in blue color. (**a**) The total structure. Right panel: Zoomed schematic of the top of the structure, where the grouped pixels are located. The length of one side of the rhombus pixel l_p is 0.5 mm. (**b**) The first pair of grouped rhombus pixels. Left panel: Schematic of transverse electric (TE) and transverse magnetic (TM) polarizations for the normal incidence. The red-dashed lines present axes that divide the hexagon into six regions. (**c**) The second, (**d**) the third, (**e**) the fourth, (**f**) the fifth, and (**g**) the hundred-and-third pairs of the rhombus pixels.

Unlike the square unit cell, the interior of the hexagon can be divided into six regions by axes that cross the center point and each vertex as red-dashed lines in Figure 1b. To maintain the axial symmetry, the rhombus pixels are grouped as shown in Figure 1b–g, for which the material properties can be set to those of the carbon or air. The axial symmetry can minimize the design complexity as well as polarization dependency of the absorbing performance. The merit of the axial symmetry will be discussed in the last paragraph in this section. For the proposed design, the total number of pixel pairs N_p is 103 and the last pair is shown in Figure 1g. The material properties of the pixels that are located at the boundary of the hexagon are set to air to insert a gap between the unit cells. The gap enables the unit cell to be distinguished from the adjacent one. Besides, it increases the series capacitance of the metapatterns, which can shift the resonance frequency downward based on the relation $f_s = 1/2\pi\sqrt{LC}$, where f_s, L, and C indicate the series resonance frequency, inductance, and capacitance of the metapattern, respectively. The effect contributes to maintain the absorbing performance at the low frequency in the target band without increasing the thickness of the acrylic substrate. Here, the sheet resistance R_s of the carbon is supposed to be 100 Ω/sq [30,39]. Because the carbon paste can be printed with a thickness 20 µm [31], the electrical conductivity σ of it can be calculated as $\sigma = 1/R_s \cdot d = 500$ S/m, where d indicates the thickness of the pattern. The relative permittivities of the carbon and air are set to 8.72 [40] and 1, respectively. The relative permeabilities of both the materials are 1.

To find the best combination of carbon pixel pairs, the genetic algorithm (GA) [30,31,33,34], i.e., a stochastic global optimization method that can evolve the FOM of a design mimicking the meiosis of the chromosome, is adopted. First, bit arrays composed with one and zero are randomly generated, for which the total number of bits N_b is the same with N_p that is 103. If the bit is one or zero, the pixel pair matched with the bit is filled with the carbon or air, respectively. The number of the random bit arrays N_a is determined to be the same with N_b, which can guarantee the diversity of the random set [30,31,34]. Among the generated random bit arrays, two of them are chosen as the best pair via a competing process using FOMs of them. FOM is calculated via the full-wave simulation, which will be described in the next paragraph. To evaluate the absorbing performance of the metamaterial absorber in the X band, FOM is defined as an average of the reflectances for the normal and 60° oblique incidences at three frequencies: 8, 10, and 12 GHz. Because the bottom side of

the proposed metamaterial absorber is blocked with PEC, the absorption A of it can be estimated by the reflectance R based on the relationship $A = 1 - R$, where 1 indicates the normalized incident power. By assuming that there exists only one absorption resonance in the X band owing to a low-Q factor of the carbon metapattern [30,39], the three-data points are sufficient to estimate the absorbing performance [41].

The full-wave simulation is conducted using COMSOL Multiphysics, a commercialized finite element method (FEM) tool. To reduce the computational cost, the three-dimensional (3D) thin carbon pixels are solved after simplifying them into two-dimensional (2D) sheets by maintaining the properties of the materials. The maximum size of the mesh is set to $\lambda_{min}/5$, where λ_{min} is the minimum wavelength of the EM wave in the X band [42]. To design the unit cell of the metamaterial absorber under the infinite-array condition, the periodic boundary condition is assigned to the side boundary of the simulation domain. By allocating a wave port at the top surface of it, the plane wave is irradiated with the incident angles 0° and 60° for both of the TE and TM polarizations. The TE and TM polarizations are the cases where the electric (E) and magnetic (H) fields are perpendicular to the plane of incidence, i.e., x–z plane, respectively, as described in Figure 1b. Based on the full-wave simulation, FOM is calculated as

$$\text{FOM} = \frac{1}{12}\sum_{i=1}^{3} R_{TE,\theta=0^\circ,f_i} + R_{TM,\theta=0^\circ,f_i} + R_{TE,\theta=60^\circ,f_i} + R_{TM,\theta=60^\circ,f_i}, \quad (1)$$

where the reflectances of TE and TM polarizations with incident angles of 0° and 60° are indicated by $R_{TE,\theta=0^\circ,f_i}$, $R_{TM,\theta=0^\circ,f_i}$, $R_{TE,\theta=60^\circ,f_i}$, and $R_{TM,\theta=60^\circ,f_i}$, respectively. The ith frequency is indicated by f_i, when the first, second, and third frequencies are matched with 8, 10, and 12 GHz, respectively.

After selecting the best pair of two bit arrays from the initial random set, the crossing and mutating operations of the GA are applied to them. For the crossing operation, a random point on the bit array is selected simultaneously for the pair. Then, the bits located after the selected point are exchanged with those included in the other bit array, and vice versa. Here, the crossing operation is repeated twenty-six times, which is approximately a quarter of the number of bits included in an array N_b. The crossing operations are repeated until they generate the same number of bit arrays N_a as the previous random set. Next, the mutating is applied by selecting random points on each bit array produced by the crossing operation. If the bit at the random point is one, it is converted to zero, and vice versa. Here, the mutating process is applied five times at each bit array.

Based on the new set of bit arrays produced by the genetic operations, the FOM of each bit array is calculated via the full-wave simulation by decoding each bit array into the metapattern, i.e., by setting the carbon or air inside the pixel pair when the bit is one or zero, respectively. After calculating FOM by averaging the reflectances of the TE and TM polarizations at the three frequencies, the best pair of metamaterial absorbers can be found by competing FOMs of them with those of others. After selecting the best pair, the metapatterns are encoded into bit arrays, and the genetic operations are applied on them again. By repeating the process, the final pair of the bit arrays is selected when the FOMs of the best pair are converged sufficiently. The best pair is selected at the thirteenth iteration based on Figure 2a, which shows FOMs of the best pair at each iteration number. Here, the iteration number for the best pair found in the initial random set is indicated by zero. Between the two bit arrays of the best pair found at the thirteenth iteration number, the first bit array is selected for which FOM is lower than that of the second one. The decoded metapattern of the selected bit array is shown in Figure 2b.

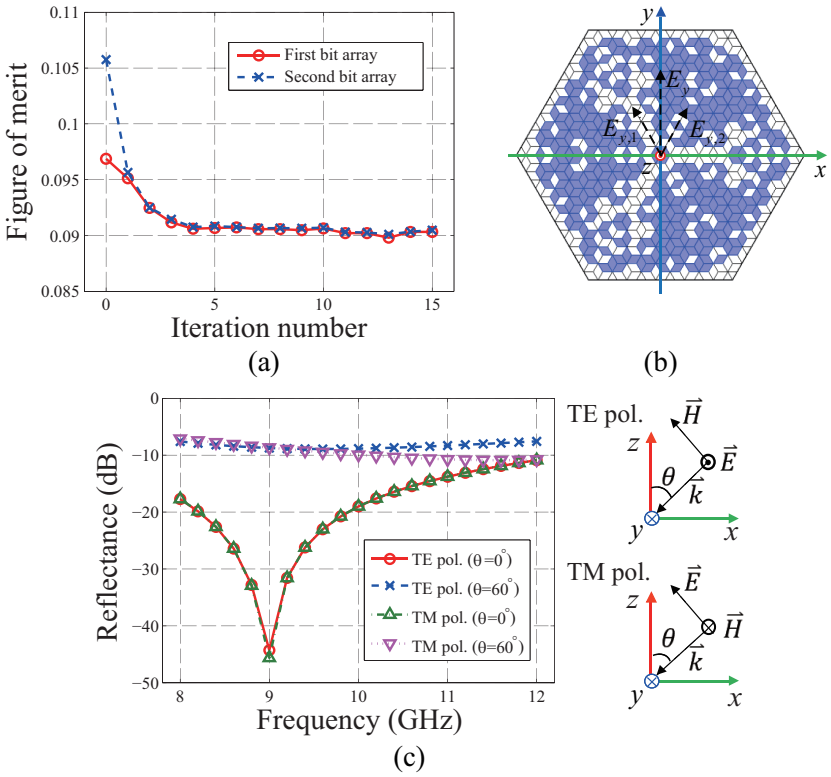

Figure 2. Optimal tiling of rhombus carbon pixels using genetic algorithm (GA). (**a**) Figure of merit vs. iteration number of GA. (**b**) Carbon metapattern decoded from the first bit array at the thirteenth iteration number. The region filled with the carbon is presented in blue color. (**c**) Full-wave simulation results of reflectance spectra of the TE and TM polarizations for the incident angles $\theta = 0°$ and $60°$.

Figure 2c shows the full-wave simulation results of Figure 2b for the TE and TM polarizations with the incident angles $\theta = 0°$ and $60°$. From the results, it can be confirmed that -10 dB reflectances are satisfied in the X band for both of the two polarizations with the normal incidence. In addition, it is confirmed that the reflectance spectra of the two polarizations are the same as each other. This is owing to the axial symmetry of the metapattern. As shown in Figure 2b, the E field of the TE polarization along with the y axis can be decomposed into two components indicated by $E_{y,1}$ and $E_{y,2}$ along with the diagonal lines of the hexagon. Owing to the symmetry of the pattern, the absorptions for the two decomposed polarizations are the same. Besides, the summation of them is the same as the absorption for the TM polarization for which the E field is, along with the x axis, coincided with the diagonal line of the hexagon. Moreover, the excellent absorption performance for the normal incidence can be found at multi-frequencies, which satisfies the condition of odd multiples of the quarter wavelength [38], $h_s = (2n-1)\lambda_n/4$, where h_s, λ_n, and n indicate the height of the substrate, the wavelength at the harmonic number n, and the positive integer, respectively. The harmonic responses can be utilized to extend the applicability of the proposed metamaterial absorber to other bands.

On the other hand, the absorbing performance of the metapattern is deteriorated for the oblique incidence with $\theta = 60°$ for both of the polarizations. This is because the electrical thickness of the substrate is abruptly reduced for the incident angle $\theta = 60°$. Because the vertical wavenumber k_v inside the substrate is expressed by $k_v = k_s \cdot \cos\theta$, where k_s is the wavenumber inside the substrate, the phase change along the vertical direction ϕ_v that is calculated by $\phi_v = k_v \cdot h_s$ should be decreased [39]. Therefore, the resonance condition utilizing the quarter-wavelength standing wave inside the substrate cannot be satisfied for the highly tilted irradiation of the EM wave.

3. Design Method for Wide-Angle Absorption

To mitigate the performance degradation for the oblique incidences, copper cylinders are added inside the acrylic substrate. The electrical conductivity σ of the copper is 5.8×10^7. Because the vertical component of the E field along with the z axis of the TM polarization in the inset of Figure 2c induces electric currents on the surfaces of the copper cylinders as well as the currents that can flow through the metapattern, an additional absorption resonance can be supported. Besides, the staple-like configurations composed of pairs of two copper cylinders connected by the metapattern on the top can be shown as square-ring loops owing to mirrored images of the electric currents by PEC [43]. Therefore, the horizontal components of the H field along with the y axis of the TM polarization, as well as H field along with the x axis of the TE polarization, induce electric currents on the surfaces of the copper cylinders via Faraday's law of induction, i.e., magnetic induction. The time-varying H fields penetrating the surfaces of the loops generate electromotive forces and induce the electric currents. Hence, additional reductions of reflectances can be expected for both of the TE and TM polarizations with the oblique incidences.

As shown in Figure 3a, a cylinder is added at the center of the hexagon and six cylinders are implanted at locations where a distance between each cylinder and the center one is equal. Unlike ref. [44], which proposes modification of a radius of a cylinder to control the additional resonance frequency, the distance between the location of each outer cylinder and the center is tuned with an interval $d_i = 2l_p \sin(\pi/3)$, where l_p indicates the length of one side of the rhombus pixel. The interval is determined to minimize the number of meshes of the FEM solver by preventing the tangential contacts of the boundaries of the pixels with those of the cylinders. For the simulation, the initial radius of each cylinder r_c is determined to 0.2 mm simultaneously. Figure 3b,c show the simulation results for the TE and TM polarizations, respectively, with the incident angles $\theta = 60^\circ$ for the various distances between the center and the outer copper cylinders. To improve the accuracy of the final design, the 3D version of Figure 2b, the carbon metapattern combined with the copper cylinders, is solved while the results shown in Figure 2c are based on the 2D version. The thickness and electrical conductivity of the 3D metapattern are set to 20 µm and 500 S/m, respectively, which are the same as those used for the 2D case.

From the results of the TE polarization with $\theta = 60^\circ$ shown in Figure 3b, a reduction of the reflectance is clearly found near the resonance frequency after implanting the copper cylinders. This is one of novelties of the proposed study distinguished from the FSS absorbers utilizing a copper cylinder, for which the reflectance spectra are fixed for the oblique incidences of the TE polarization [39,44]. From Figure 3b, it can be confirmed that the resonance frequency of the magnetic induction via the staple-like structures can be controlled by adjusting the distance between the cylinders. It is observed that the resonance frequency is shifted downward as the distance between the center and outer copper cylinders is increased. This is because the length of the staple-like structure related with the inductance L of it is determined by the distance between the cylinders under the condition that the metapattern and the pair of two copper cylinders are connected with each other. Even though the effect of the copper cylinders is confirmed for the TE polarization, there do not exist distinct variations in the levels of the reflectance spectra. Therefore, the optimal distance is determined considering the results of the TM polarization. From the results of the TM polarization with $\theta = 60^\circ$ shown in Figure 3c, it is found that the distance of $3d_i$ is the optimal one considering the level of the reflectance. For this case, two absorption mechanisms coexist, i.e., the magnetic induction occurring from the H field along with the y axis, as well as the current induced by the E field decomposed along with the z axis. Therefore, the optimal distance is found via the parametric study using the full-wave simulation without expecting the trend of the spectrum.

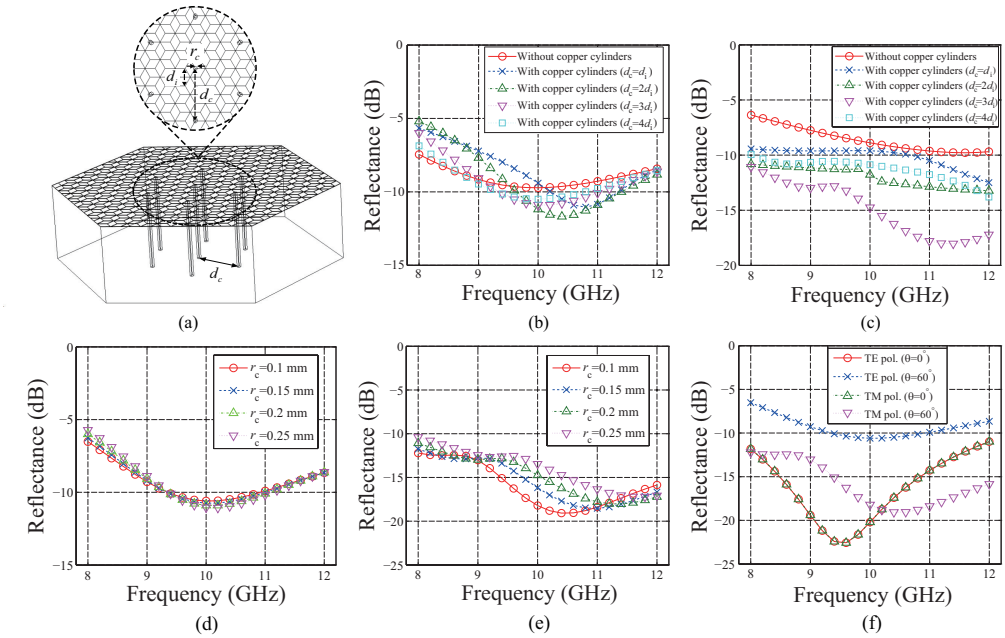

Figure 3. Simulation results of parametric studies of the metamaterial absorber including copper cylinders inside the acrylic substrate. (**a**) Schematic of implanted copper cylinders inside the acrylic substrate. Upper panel: Zoomed top surface of the schematic for which d_i, d_c, and r_c, are 0.866, 2.598, and 0.1 mm, respectively. Full-wave simulation results of reflectance spectra depend on d_c for the oblique incidence angle $\theta = 60^\circ$ with (**b**) TE and (**c**) TM polarizations. Full-wave simulation results of reflectance spectra depend on r_c for the oblique incidence angle $\theta = 60^\circ$ with (**d**) TE and (**e**) TM polarizations. (**f**) Full-wave simulation results of reflectance spectra of the TE and TM polarizations for $\theta = 0^\circ$ and 60° utilizing $d_c = 3d_i = 2.598$ mm and $r_c = 0.1$ mm.

To investigate an effect of the radii of the cylinders on the reflectance spectra, the simulations are conducted by changing the radii of them simultaneously from 0.1 to 0.25 mm with an interval of 0.05 mm. As shown in Figure 3d, there do not exist distinguishable differences in the reflectance spectra for the TE polarization with $\theta = 60^\circ$. This shows that the resonance frequency of the magnetic induction generated by the H field parallel with the x axis is not affected by the radii of the copper cylinders. However, it is found in Figure 3e that the resonance frequency is shifted upward when the radii of the cylinders are increased for the TM polarization with $\theta = 60^\circ$. This is well matched with the trend of the plasma frequency vs. the radius of a metallic cylinder [1,44]. This is evidence of the mechanism that the resonance is generated by the decomposed E field parallel with the z axis inducing the oscillating electric currents, i.e., plasmons [1], on the surface of the copper cylinders. From Figure 3e, the optimal radii of the cylinders r_c is determined as 0.1 mm. Even though it can be expected that the reflectance level is decreased further as the radii are reduced, the smallest size of them is set to 0.1 mm considering the possibility of the fabrication. The cylindrical holes with radii 0.1 mm can be perforated using a milling process, and the holes can be filled with copper wires that have the same radii as those of the holes. For the fabrication of the carbon metapattern, a screen-printing method [26,31,45] can be utilized. It is well established that the sheet resistance 100 Ω/sq can be achieved by controlling the sintering time of the printed carbon pattern [26,31]. To make an electrical connection between the copper cylinders and carbon metapattern, silver paste can be applied at the interface of them, which can connect two different conducting materials via the soldering process [25]. The fabrication of the design will be investigated in future work.

Figure 3f shows the simulation results for the TE and TM polarizations with $\theta = 0^\circ$ and 60° after implanting copper cylinders inside the substrate with the optimal conditions $d_c = 3d_i$ and $r_c = 0.1$ mm. From the results, the reflectance spectra of the TE and TM polarizations for the normal incidence still remain below -10 dB in the X band. Even

though the reflectance spectra of the TE and TM polarizations with $\theta = 60^\circ$ are reduced compared with the results in Figure 2c near the center frequency 10 GHz, it is found that the reflectance levels of the TE polarization at the edges of the X band are not suppressed sufficiently compared with those of the TM case. To attain the broadband and wide-angle absorbing performance for both of the polarizations, the combination of carbon rhombus pixels is optimized further by applying GA operations adaptively [34] after fixing the conditions of the implanted copper cylinders. As an initial condition for the adaptive GA operations, the pair of bit arrays selected at the thirteenth iteration in Figure 2a are used. To minimize the reflectances at the lowest and highest frequencies of the X band simultaneously for the TE polarization with $\theta = 60^\circ$, FOM is calculated as

$$\text{FOM} = \frac{1}{2}\left(R_{TE,\theta\,=\,60^\circ,f\,=\,8\text{ GHz}} + R_{TE,\theta\,=\,60^\circ,f\,=\,12\text{ GHz}}\right), \quad (2)$$

where the reflectances of TE polarization with the incident angle $\theta = 60^\circ$ at 8 and 12 GHz are indicated by $R_{TE,\theta=60^\circ,f=8\text{ GHz}}$ and $R_{TE,\theta=60^\circ,f=12\text{ GHz}}$, respectively. By modifying FOM adaptively by considering the reflectance spectra in Figure 3f, a new combination of carbon pixels can be found that enhances the absorption for the TE polarization with $\theta = 60^\circ$. However, the other performances especially for the TM polarization with $\theta = 60^\circ$ can be degraded as the iteration number is increased. Hence, the adaptive GA operations are truncated at the seventh iteration number, which is less than that used for the design of the intermediate metapattern in Figure 2a.

Figure 4a shows FOMs of the best pair of two bit arrays at each iteration step of the adaptive GA operations. Here, the zeroth step indicates the initial condition utilizing the best pair found at the thirteenth iteration number of the previous design in Figure 2a. From Figure 4a, it is found that FOM is minimized at the fifth iteration from the initial condition. Between the two bit arrays of the best pair, the first bit array is selected for which FOM is lower than that of the second one. The decoded metamaterial absorber of the selected bit array is shown in Figure 4b. The upper panel of Figure 4b shows the top surface of the carbon metapattern. The metamaterial absorber includes the same copper cylinders described in the previous paragraph. Here, to verify the accuracy of the design, simulation results calculated by another commercialized FEM solver, HFSS, are compared with the results calculated by Comsol Multiphysics by benchmarking a reference paper that verifies the novelty of the design via simulation results calculated by two different numerical simulators, CST and HFSS [44]. Figure 4c shows the schematic of the same metamaterial absorber using HFSS. The upper panel of Figure 4c shows the same carbon metapattern as Figure 4b.

Figure 4d shows the reflectance spectra of the metamaterial absorber calculated using Comsol Multiphysics and HFSS for the TE and TM polarizations with $\theta = 0^\circ$ and 60°. Based on the well-matched trends of the reflectance spectra of Comsol Multiphysics and HFSS, the accuracy of the design can be verified. From the results, it can be found that the reflectance levels of the TE polarization with $\theta = 60^\circ$ are dramatically reduced at the edges of the X band. This is not only because the magnetic induction is supplied by the copper cylinders, but also because FOM for the adaptive design is focused on the reflectance of the TE polarization with $\theta = 60^\circ$ using Equation (2). Besides, a broad -10 dB bandwidth is confirmed from 8.8 to 11.6 GHz simultaneously in all cases, for which the fractional bandwidth is 27.5%. The fractional bandwidth is calculated by the ratio between the -10 dB bandwidth and the center frequency of it. Figure 4e,f show the electric current densities in the carbon metapattern for the TE and TM polarizations at $f = 9.6$ and 11.8 GHz, respectively. The frequencies 9.6 and 11.8 GHz are the dominant resonance frequencies for the TE and TM polarizations, respectively, found in Figure 4d. From the results, it is clearly confirmed that the electric currents are strongly induced in the three pairs of the two cylinders connected by the metappatern for both of the polarizations.

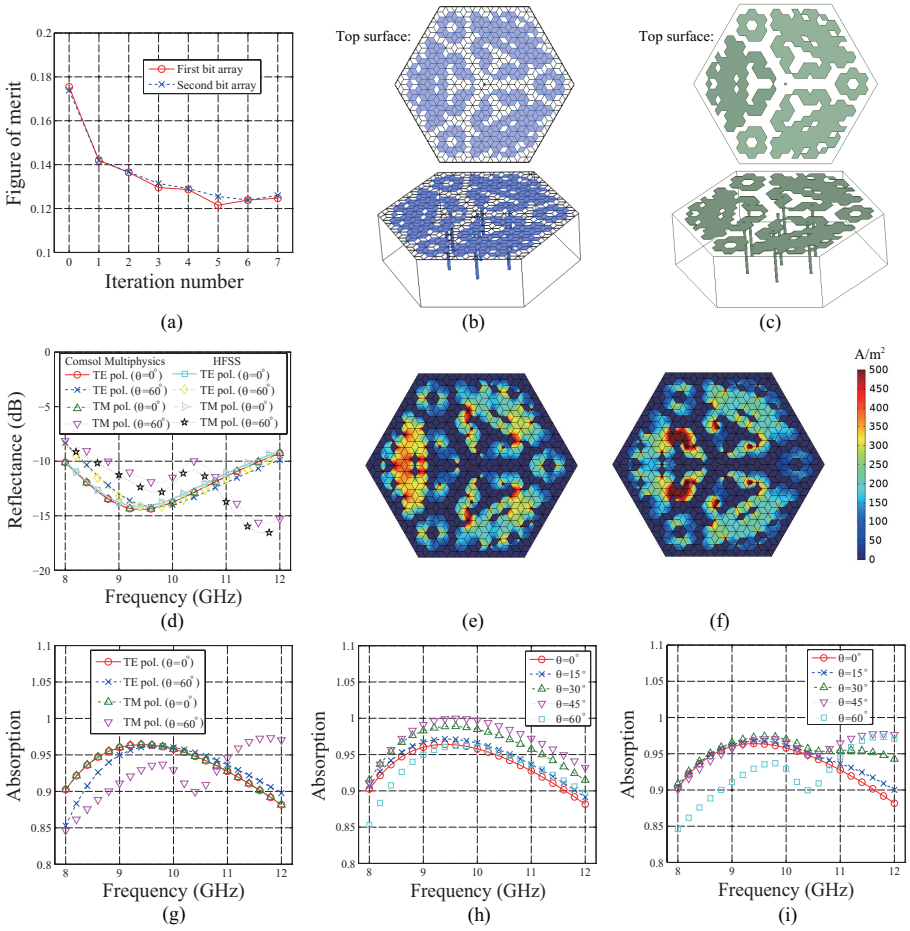

Figure 4. Adaptively optimized metamaterial absorber via tiling of rhombus carbon pixels using GA considering implantation of the copper cylinders inside the acrylic substrate. (**a**) Figure of merit vs. iteration number of adaptive GA operations. (**b**) Schematic of metamaterial absorber decoded from the first bit array at the fifth iteration number. Upper panel: Top surface. (**c**) Schematic of the same metamaterial absorber using HFSS. Upper panel: Top surface. (**d**) Full-wave simulation results of reflectance spectra of the TE and TM polarizations for the incident angles $\theta = 0°$ and 60° using Comsol Multiphysics and HFSS. Electric current densities of (**e**) TE polarization at f = 9.6 GHz and (**f**) TM polarization at f = 11.8 GHz. (**g**) Absorption spectra of the TE and TM polarizations for the incident angles $\theta = 0°$ and 60°. Absorption spectra for the incident angles from $\theta = 0°$ and 60° with an interval 15° with (**h**) TE and (**i**) TM polarizations.

Table 1 shows the comparisons of the reflectance bandwidths as well as the ranges of incident angle of the proposed metamaterial absorber for the TE and TM polarizations with those of other recently reported metamaterial or FSS absorbers. Because the bandwidth can be proportionally increased with the thickness of the substrate [46], the bandwidths are compared with those of a metamaterial absorber utilizing eight resistive arms [20], for which the electrical length of the substrate thickness is the same as that of the proposed one. From Table 1, it can be found that the bandwidths of the proposed metamaterial absorber are as broad as that of the referenced paper [20] for the TE polarization and much broader than that for the TM polarization in the entire range of incident angle from 0° to 60°. In addition, it is found that the bandwidths of the proposed metamaterial absorber are much broader than those of an FSS absorber using resistively loaded quadruple hexagonal loops [32]. Moreover, it is confirmed that the ranges of incident angle are slightly broader than those of the dispersion-engineered metamaterial absorber [28] for both the TE and TM polarizations. To enhance the bandwidth further, metamaterial absorbers composed of multilayer metapatterns [31,47] and copper cylinders can be considered as a possible candidate, and a study for the design will be the subject of future work.

Table 1. Comparisons of simulated −10 dB reflectance bandwidths (BWs) of single-layer metamaterial or frequency-selective surface absorbers for TE and TM polarizations. The incident angle and the wavelength at the center frequency in the substrate are indicated by θ and λ_g, respectively. NA: Not applicable.

	TE		TM		Thickness of Substrate (λ_g)	Unit-Cell Shape
	Fractional BW (%)	θ	Fractional BW (%)	θ		
[20]	31.68 (8.5–11.7 GHz)	0°–60°	17.54 (10.4–12.4 GHz)	0°–60°	0.22 (3 mm)	Square
[28]	48.48 (2.25–3.69 GHz)	0°–50°	48.48 (2.25–3.69 GHz)	0°–50°	NA (13 mm)	Square
[32]	15.63 (16.4–19.18 GHz)	0°–45°	15.63 (16.4–19.18 GHz)	0°–45°	0.23 (3 mm)	Hexagon
This work	32 (8.4–11.6 GHz)	0°–60°	27.45 (8.8–11.6 GHz)	0°–60°	0.22 (4 mm)	Hexagon

Even though the increment of the absorption A can be estimated by the reduction of the reflectance R based on the relation $A = 1 - R$, non-negligible leakage of power out of the specular direction owing to diffusion [47,48] or high-order reflection modes [49] by the metapattern may deteriorate the accuracy of the estimation. Therefore, the absorptions are calculated precisely for the TE and TM polarizations with $\theta = 0°$ and $\theta = 60°$. To this end, the dissipated power is calculated by integrating the dissipated power density with respect to the volume of each part of the metamaterial absorber, and the total dissipated power is calculated by a summation of dissipated power at each part [50]. The absorption is calculated by dividing the total dissipated power by the input power. The input power P_{in} can be calculated by integrating the input time-averaged power density with the area of the unit cell,

$$P_{in} = \frac{3}{2\eta} E_0^2 l_s^2 \sin\frac{\pi}{3}\cos\theta, \quad (3)$$

where the electric field intensity, the length of one side of the hexagonal unit cell, the vertical incident angle, and the intrinsic impedance of the air are indicated by E_0, l_s, θ, and η, respectively. Here, E_0, l_s, and η are 1 V/m, 7.5 mm, and 377 Ω, respectively. Figure 4g shows the calculated absorption spectra based on the ratios between the total dissipated and input powers. From Figure 4g, the 90% absorption bandwidth is confirmed from 8.8 to 11.6 GHz, for which the fractional bandwidth is 27.5%, which is the same as the −10 dB reflectance bandwidth. Figure 4h,i show the absorption spectra of the TE and TM polarizations, respectively, for the oblique incident angles θ from 0° to 60° with an interval 15°. From the results, it is clearly confirmed that the absorption bandwidths for the oblique incidences from $\theta = 15°$ to 45° are as broad as that confirmed at both of the incident angles 0° and 60°.

4. Conclusions

A design for a broadband and wide-angle hexagonal metamaterial absorber was proposed based on the optimal tiling of rhombus carbon pixels using the GA and implantation of copper cylinders inside the acrylic substrate. It was confirmed that the broadband absorption for both of the TE and TM polarizations with the normal incidence can be achieved via the optimal tiling of carbon rhombus pixels. By adding copper cylinders at the center and six positions around it, pairs of two cylinders combined with the metapattern form staple-like configurations. The proposed staple-like configurations can utilize the resonances related not only with the plasmons for the obliquely incident TM polarization, but also the magnetic induction for the obliquely incident TE polarization. The additional resonances enhance the reductions of the reflectance levels for both of the obliquely incident TE and TM polarizations. This is a novelty of the proposed design distinguished from the referenced EM absorbers utilizing a copper cylinder [39,44], which are only effective for obliquely incident TM polarization. Finally, GA operations were applied on the carbon tiles adaptively to enhance the absorption bandwidth for the TE polarization with $\theta = 60°$, for which the performance is degraded at the edges of the X band. It was clearly found that the bandwidth is effectively enlarged by tiling the carbon pixels adaptively using the GA. Based on full-wave simulations, the −10 dB reflectance as well as 90% absorption bandwidths were confirmed from 8.8 to 11.6 GHz, for which the fractional bandwidth was

27.5% for the both of the polarizations with the incident angles from 0° to 60°. From the well-matched reflectance and absorption bandwidths, it can be verified rigorously that the suppressions of the reflectance levels are owing to the increments of the absorptions via the proposed metamaterial absorber. The proposed design method based on optimal tiling of carbon pixels and implantation of copper cylinders could open a way to design a broadband, wide-angle, and polarization-insensitive EM absorber. Besides, the proposed metamaterial absorber could be applied to reduce the radar cross-section of surveillance and reconnaissance platforms such as square pyramidal integrated masts mounted on destroyers [25] based on the merit of the hexagonal shape of the unit cell as well as broadband and wide-angle absorbing performances.

Author Contributions: Conceptualization, Y.K. and J.-H.L.; design and simulation, Y.K.; analysis, Y.K. and J.-H.L.; manuscript preparation, Y.K.; manuscript revision, J.-H.L.; supervision, J.-H.L. All authors have read and agreed to the published version of the manuscript.

Funding: This work was supported by the Basic Science Research Program through the National Research Foundation of Korea (NRF) funded by the Ministry of Education (2015R1A6A1A03031833) and by the MSIT (Ministry of Science and ICT), Korea, under the ITRC (Information Technology Research Center) support program (IITP-2021-2016-0-00291) supervised by the IITP (Institute for Information & Communications Technology Planning & Evaluation).

Institutional Review Board Statement: Not applicable.

Informed Consent Statement: Not applicable.

Conflicts of Interest: The authors declare no conflicts of interest.

References

1. Pendry, J.B.; Holden, A.J.; Stewart, W.J.; Youngs, I. Extremely low frequency plasmons in metallic mesostructures. *Phys. Rev. Lett.* **1996**, *76*, 4773. [CrossRef] [PubMed]
2. Pendry, J.B.; Holden, A.J.; Robbins, D.J.; Stewart, W.J. Magnetism from conductors and enhanced nonlinear phenomena. *IEEE Trans. Microw. Theory Tech.* **1999**, *47*, 2075. [CrossRef]
3. Smith, D.R.; Kroll, N. Negative refractive index in left-handed materials. *Phys. Rev. Lett.* **2000**, *85*, 2933. [CrossRef] [PubMed]
4. Sanada, A.; Caloz, C.; Itoh, T. Novel zeroth-order resonance in composite right/left-handed transmission line resonators. In Proceedings of the 2003 Asia-Pacific Microwave Conference, Seoul, Korea, 4–7 November 2003; Volume 3; pp. 1588–1591.
5. Park, J.-H.; Ryu, Y.-H.; Lee, J.-G.; Lee, J.-H. Epsilon negative zeroth-order resonator antenna. *IEEE Trans. Antennas Propag.* **2007**, *55*, 3710–3712. [CrossRef]
6. Park, J.-H.; Ryu, Y.-H.; Lee, J.-H. Mu-zero resonance antenna. *IEEE Trans. Antennas Propag.* **2010**, *58*, 1865–1875. [CrossRef]
7. Lee, J.-G.; Kim, D.-J.; Lee, J.-H. Compact penta-band dual ZOR antenna for mobile applications. *Int. J. Antennas Propag.* **2016**, *2016*, 6461805. [CrossRef]
8. Schurig, D.; Mock, J.J.; Justice, B.J.; Cummer, S.A.; Pendry, J.B.; Starr, A.F.; Smith, D.R. Metamaterial electromagnetic cloak at microwave frequencies. *Science* **2006**, *314*, 977–980. [CrossRef] [PubMed]
9. Liu, R.; Ji, C.; Mock, J.J.; Chin, J.Y.; Cui, T.J.; Smith, D.R. Broadband ground-plane cloak. *Science* **2009**, *323*, 366–369. [CrossRef]
10. Ma, H.F.; Jiang, W.X.; Yang, X.M.; Zhou, X.Y.; Cui, T.J. Compact-sized and broadband carpet cloak and free-space cloak. *Opt. Express* **2009**, *17*, 19947–19959. [CrossRef]
11. Kim, Y.; Seo, I.; Koh, I.-S.; Lee, Y. Design method for broadband free-space electromagnetic cloak based on isotropic material for size reduction and enhanced invisibility. *Opt. Express* **2016**, *24*, 22708–22717. [CrossRef]
12. Kim, Y.; Deng, T.; Jiang, W.X.; Cui, T.J.; Lee, Y.; Qiu, C.-W. Robust control of a multifrequency metamaterial cloak featuring intrinsic harmonic selection. *Phys. Rev. Appl.* **2018**, *10*, 044027. [CrossRef]
13. Landy, N.I.; Sajuyigbe, S.; Mock, J.J.; Smith, D.R.; Padilla, W.J. Perfect metamaterial absorber. *Phys. Rev. Lett.* **2008**, *100*, 207402. [CrossRef]
14. Tao, H.; Kadlec, E.A.; Strikwerda, A.C.; Fan, K.; Padilla, W.J.; Averitt, R.D.; Shaner, E.A.; Zhang, X. Microwave and terahertz wave sensing with metamaterials. *Opt. Express* **2011**, *19*, 21620–21626. [CrossRef]
15. Lee, J.; Lim, S. Bandwidth-enhanced and polarisation-insensitive metamaterial absorber using double resonance. *Electron. Lett.* **2011**, *47*, 8–9. [CrossRef]
16. Xu, H.-X.; Wang, G.-M.; Qi, M.-Q.; Liang, J.-G.; Gong, J.-Q.; Xu, Z.-M. Triple-band polarization-insensitive wide-angle ultra-miniature metamaterial transmission line absorber. *Phys. Rev. B* **2012**, *86*, 205104. [CrossRef]
17. Savinov, V.; Fedotov, V.A.; Groot, P.D.; Zheludev, N.I. Radiation-harvesting resonant superconducting sub-THz metamaterial bolometer. *Supercond. Sci. Technol.* **2013**, *26*, 084001. [CrossRef]

18. Fan, K.; Suen, J.Y.; Liu, X.; Padilla, W.J. All-dielectric metasurface absorbers for uncooled terahertz imaging. *Optica* **2017**, *4*, 601–604. [CrossRef]
19. Beeharry, T.; Yahiaoui, R.; Selemani, K.; Ouslimani, H.H. A dual layer broadband radar absorber to minimize electromagnetic interference in radomes. *Sci. Rep.* **2018**, *8*, 382. [CrossRef] [PubMed]
20. Nguyen, T.T.; Lim, S. Design of metamaterial absorber using eight-resistive-arm cell for simultaneous broadband and wide-Incidence-angle absorption. *Sci. Rep.* **2018**, *8*, 6633. [CrossRef]
21. Jeong, H.; Nguyen, T.T.; Lim, S. Meta-dome for broadband radar absorbing structure. *Sci. Rep.* **2018**, *8*, 17893. [CrossRef]
22. Zhou, Z.; Zhou, T.; Zhang, S.; Shi, Z.; Chen, Y.; Wan, W.; Li, X.; Chen, X.; Corder, S.N.G.; Fu, Z.; et al. Multicolor T-ray imaging using multispectral metamaterials. *Adv. Sci.* **2018**, *5*, 1700982. [CrossRef]
23. Lu, T.; Zhang, D.; Qiu, P.; Lian, J.; Jing, M.; Yu, B.; Wen, J. Ultrathin terahertz dual-band perfect metamaterial absorber using asymmetric double-split rings resonator. *Symmetry* **2018**, *10*, 293. [CrossRef]
24. Elsharabasy, A.; Bakr, M.; Deen, M.J. Wide-angle, wide-band, polarization-insensitive metamaterial absorber for thermal energy harvesting. *Sci. Rep.* **2020**, *10*, 16215. [CrossRef]
25. Kim, Y.; Kim, D.; Lee, S.-H.; Seo, M.; Jung, H.-J.; Kang, B.; Lee, S.-M.; Lee, H.-J. Single-layer metamaterial bolometer for sensitive detection of low-power terahertz waves at room temperature. *Opt. Express* **2020**, *28*, 17143–17152. [CrossRef]
26. Ra, Y.E.; Kim, Y.; Jung, H.J.; Park, P.; Jo, J.; Lee, J.; Kim, M.; Jung, J.; Lee, G.-M.; Lee, J.-H.; Lee, H.-J. Verification of durability of electromagnetic metamaterial absorber in temperature varying environment for its application to integrated mast of next generation destroyer. *J. Inst. Korean. Electr. Electron. Eng.* **2020**, *24*, 347–353.
27. Ha, D.T.; Hanh, V.T.H.; Tung, B.S.; Hien, N.T.; Dung, D.N.; Khuyen, B.X.; Chen, L.Y.; Lee, Y.; Lam, V.D. Ultrathin hybrid absorber based on high-order metamaterial. *J. Opt.* **2021**, *23*, 095101. [CrossRef]
28. Shi, T.; Jin, L.; Han, L.; Tang, M.-C.; Xu, H.-X.; Qiu, C.-W. Dispersion-engineered, broadband, wide-angle, polarization-independent microwave metamaterial absorber. *IEEE Trans. Antennas Propag.* **2021**, *69*, 229–238. [CrossRef]
29. Xu, H.-X.; Wang, M.; Hu, G.; Wang, S.; Wang, Y.; Wang, C.; Zeng, Y.; Li, J.; Zhang, S.; Huang, W. Adaptable invisibility management using kirigami-inspired transformable metamaterials. *Research* **2021**, *2021*, 9806789. [CrossRef]
30. Kim, Y.; Lee, S.-G.; Lee, J.-H. Optimal design of broadband hexagonal electromagnetic metamaterial absorber unit cells. *J. Korean Inst. Electromagn. Eng. Sci.* **2021**, *32*, 533–540. [CrossRef]
31. Kim, Y.; Park, P.; Jo, J.; Lee, J.; Jeong, L.; Shin, J.; Lee, J.-H.; Lee, H.-J. Ultrawideband electromagnetic metamaterial absorber utilizing coherent absorptions and surface plasmon polaritons based on double layer carbon metapatterns. (under review)
32. Zabri, S.N.; Cahill, R.; Schuchinsky, A. Compact FSS absorber design using resistively loaded quadruple hexagonal loops for bandwidth enhancement. *Electron. Lett.* **2015**, *51*, 162–164. [CrossRef]
33. Haupt, R.L. An introduction to genetic algorithms for electromagnetics. *IEEE Antennas. Propag. Mag.* **1995**, *37*, 7–15. [CrossRef]
34. Jafar-Zanjani, S.; Inampudi, S.; Mosallaei, H. Adaptive genetic algorithm for optical metasurfaces design. *Sci. Rep.* **2018**, *8*, 11040. [CrossRef] [PubMed]
35. Baake, M.; Gähler, F.; Grimm, U. Hexagonal inflation tilings and planar monotiles. *Symmetry* **2012**, *4*, 581–602. [CrossRef]
36. Chung, P.N.; Fernandez, M.A.; Li, Y.; Mara, M.; Morgan, F.; Plata, I.R.; Shah, N.; Vieira, L.S.; Wikner, E. Isoperimetric pentagonal tilings. *N. Am. Math. Soc.*, **2012**, *59*, 632–640. [CrossRef]
37. Eyraud, C.; Geffrin, J.-M.; Litman, A.; Tortel, H. Complex permittivity determination from far-field scattering patterns. *IEEE Antennas Wirel. Propag. Lett.* **2014**, *14*, 309–312. [CrossRef]
38. Tischler, J.R.; Bradley, M.S.; Bulović, V. Critically coupled resonators in vertical geometry using a planar mirror and a 5 nm thick absorbing film. *Opt. Lett.* **2006**, *31*, 2045–2047. [CrossRef]
39. Tretyakov, S.A.; Maslovski, S.I. Thin absorbing structure for all incidence angles based on the use of a high-impedance surface. *Microw. Opt. Technol. Lett.* **2003**, *38*, 175–178. [CrossRef]
40. Reedijk, J.A.; Martens, H.C.F.; Smits, B.J.G.; Brom, H.B. Measurement of the complex dielectric constant down to helium temperatures. II. Quasioptical technique from 0.03 to 1 THz. *Rev. Sci. Instrum.* **2000**, *71*, 478–481. [CrossRef]
41. Kim, Y.; Koh, I.-S.; Lee, Y. A finite-difference time-domain normal mode method for broadband transmission loss predictions. *Acta Acust. United Acust.* **2017**, *103*, 758–766. [CrossRef]
42. Deibel, J.A.; Escarra, M.; Berndsen, N.; Wang, K.; Mittleman, D.M. Finite-element method simulations of guided wave phenomena at terahertz frequencies. *Proc. IEEE* **2007**, *95*, 1624–1640 [CrossRef]
43. Zhang, S.; Fan, W.; Minhas, B.K.; Frauenglass, A.; Malloy, K.J.; Brueck, S.R.J. Midinfrared resonant magnetic nanostructures exhibiting a negative permeability *Phys. Rev. Lett.* **2005**, *94*, 037402. [CrossRef]
44. Luukkonen, O.; Costa, F.; Simovski, C.R.; Monorchio, A.; Tretyakov, S.A. A thin electromagnetic absorber for wide incidence angles and both polarizations. *IEEE Trans. Antennas Propag.* **2009**, *57*, 3119–3125. [CrossRef]
45. Khan, S.; Tinku, S.; Lorenzelli, L.; Dahiya, R.S. Flexible tactile sensors using screen-printed p(vdf-trfe) and mwcnt/pdms composites. *IEEE Sens. J.* **2015**, *15*, 3146–3155. [CrossRef]
46. Rozanov, K.N. Ultimate thickness to bandwidth ratio of radar absorbers. *IEEE Trans. Antennas Propag.* **2000**, *48*, 1230–1234. [CrossRef]
47. Zhang, C.; Zhao, J.; Zhang, B.H.; Song, R.G.; Wang, Y.C.; He, D.P.; Cheng, Q. An optically transparent metasurface for broadband microwave antireflection. *ACS Appl. Mater. Interfaces* **2021**, *13*, 7698–7704. [CrossRef] [PubMed]

48. Xu, H.-X.; Zhang, L.; Kim, Y.; Wang, G.-M.; Zhang, X.-K.; Sun, Y.; Ling, X.; Liu, H.; Chen, Z.; Qiu, C.-W. Wavenumber-splitting metasurfaces achieve multichannel diffusive invisibility. *Adv. Opt. Mater.* **2018**, *6*, 1800010. [CrossRef]
49. Guo, Q.; Hao, F. Comments on "Wideband microwave absorber comprising metallic split-ring resonators surrounded with E-shaped fractal metamaterial". *IEEE Access* **2021**, *9*, 121302–121304. [CrossRef]
50. Assimonis, S.D.; Fusco, V. Polarization insensitive, wide-angle, ultra-wideband, flexible, resistively loaded, electromagnetic metamaterial absorber using conventional inkjet-printing technology. *Sci. Rep.* **2019**, *9*, 12334. [CrossRef] [PubMed]